Methodology for the Redesign of Compressor Blades Undergoing Nonlinear Structural Interactions: Application to Blade-tip/Casing Contacts

Solène Kojtych, Florence Nyssen, Charles Audet, Alain Batailly

POLYTECHNIQUE MONTRÉAL
UNIVERSITÉ D'INGÉNIERIE

LABORATOIRE D'ANALYSE VIBRATOIRE ET ACOUSTIQUE

Methodology for the Redesign of Compressor Blades Undergoing Nonlinear Structural Interactions: Application to Blade-tip/Casing Contacts

Solène Kojtych[1], Florence Nyssen[1], Charles Audet[2], Alain Batailly[1]

Abstract

Over the past decade, the drive towards more efficient aircraft engines has pushed the boundaries of operating ranges far beyond a linear structural context. Nonlinear interfaces, such as blade-tip/casing contacts, are to be expected in nominal operating conditions. However, current blade design methodologies still rely on empirical structural considerations, often linear, which may lead to costly redesign operations. This work aims at proposing a methodology for the redesign of blades undergoing nonlinear structural interactions. A three-step redesign process is considered: (1) parameterization of an existing blade, (2) update of blade parameters with respect to a surrogate performance criterion and (3) performance check of the optimized blade. An original two-way parameterization method is proposed to parameterize existing blades and generate models from blade parameters. As a proof-of-concept, the redesign of the NASA compressor blade rotor 37 and fan blade rotor 67 with respect to blade-tip/casing contacts is considered. High-fidelity parameterized models of the initial blades are obtained and their dynamic response to contact interactions are analyzed. Geometries are updated with respect to their clearance consumption, as its minimization has shown beneficial effects on the considered contact interactions. The proposed methodology allows to better assess the relevance of this performance criterion in the context of blade-tip/casing contacts.

Keywords

nonlinear structural interactions, blade redesign, compressor blades, blade-tip/casing contacts

1 - Department of Mechanical Engineering, Polytechnique Montréal, P.O. Box 6079, Succ. Centre-Ville, Montréal, Québec, Canada H3C 3A7
2 - Department of Mathematics and Industrial Engineering, Polytechnique Montréal, P.O. Box 6079, Succ. Centre-Ville, Montréal, Québec, Canada H3C 3A7

Méthodologie pour la reconception d'aubes de compresseurs soumises à des interactions de contact non linéaires : application aux contacts aube/carter

Solène Kojtych[1], Florence Nyssen[1], Charles Audet[2], Alain Batailly[1]

Résumé

Ces dix dernières années, la volonté d'améliorer l'efficacité des moteurs d'avions a conduit à repousser les frontières des conditions opératoires bien au-delà d'un contexte structurel linéaire. Les interfaces non linéaires, telles que l'interface de contact aube/carter, sont présentes en conditions opératoires nominales. Pourtant, les méthodologies de conception d'aubes actuelles reposent encore sur des considérations structurales empiriques, souvent linéaires, qui peuvent mener à de coûteuses opérations de reconception. L'objectif de ce travail est de proposer une méthodologie pour la reconception d'aubes de compresseurs soumises à des interactions structurales non linéaires. Un processus de reconception en trois étapes est considéré : (1) la paramétrisation d'une aube existante, (2) la mise à jour de l'aube en fonction d'un critère de performance substitut et (3) la vérification des performances de l'aube optimisée. Une méthode de paramétrisation bi-directionnelle originale est proposée: elle permet à la fois de paramétrer des aubes existantes et de générer des modèles à partir de paramètres d'aubes. Comme preuve de concept, la reconception par rapport aux contacts aubes/carter des aubes de la NASA rotor 37 (compresseur) et rotor 67 (soufflante) est effectuée. Des modèles paramétrés haute-fidélité des aubes initiales sont obtenus et leur réponse dynamique à des interactions de contact est analysée. Les géométries sont mises à jour en fonction de leur consommation de jeu car la minimisation de cette quantité a conduit à des effets bénéfiques sur les interactions de contact considérées. La méthodologie proposée permet de mieux évaluer la pertinence de ce critère de performance dans le contexte des interactions de contact aube/carter.

Mots-clés

interactions structurales non linéaires, reconception d'aubes, aubes de compresseur, contacts aube/carter

1 - Département de génie mécanique, Polytechnique Montréal, P.O. Box 6079, Succ. Centre-Ville, Montréal, Québec, Canada H3C 3A7
2 - Département de mathématiques et génie industriel, Polytechnique Montréal, P.O. Box 6079, Succ. Centre-Ville, Montréal, Québec, Canada H3C 3A7

1 Introduction

Nonlinear structural interactions have been the focus of a vast amount of research investigations over the past years [1]. Indeed, the current lack of unified theoretical framework in which mechanical systems featuring nonlinear interfaces may be analyzed drove a variety of research projects in order to better understand, predict, and ideally mitigate nonlinear structural interactions [2, 3, 4, 5]. For specific mechanical components such as aircraft engine blades, nonlinear structural interactions constitute a major roadblock for designers for two reasons: (1) aircraft engine blades feature several nonlinear interfaces [6, 7], which makes it extremely difficult to accurately predict their dynamics [3, 8], and (2) the recent drive towards the reduction of aircraft engines' environmental footprint imposes design constraints, that makes it essential to account for nonlinear structural interactions which may now occur in non-accidental configurations [9, 10]. In this context, new design tools and methodologies [11, 12] are required to design blades more robust to nonlinear structural interactions.

While researchers are currently focusing on the development of design guidelines and criteria to enhance the robustness of aircraft engine blades to nonlinear structural interactions [13], aircraft engine blades are still currently designed using empirical guidelines—oftentimes related to linear structural considerations—that may fail in the context of specific nonlinear structural interactions. In that case, redesign operations [14] are called for, with a potentially very costly impact as planes may be grounded. Preventing these redesign operations essentially depends on two key elements: (1) the ability to easily and efficiently update a blade design, and (2) physically relevant design criteria to help improve the blade's dynamics in the context of a specific interaction.

This paper focuses specifically on nonlinear structural interactions that may arise following blade-tip/casing contacts within an aircraft engine compressor [12, 15]. Mitigating such interactions at the compressor stage is indeed strategic for engineers as it is inherently tied to the reduction of nominal operating clearances which prevents parasitic leakage flows. Previous investigations have underlined that the redesign of a high-pressure compressor blade can successfully yield an increased robustness to structural contacts [16]. In particular, the blade was optimized with respect to its clearance consumption [17]—which quantifies how the blade-tip/casing clearance evolves as the blade vibrates along one of its free-vibration modes—and much lower amplitudes of vibration were numerically predicted for the redesigned blade. Based on this work, a blade parameterization was later proposed for academic blade models and systematic optimization of these profiles with respect to their clearance consumption underlined the relevance of this criterion [18].

The work presented in this paper expands the scope of these previous studies in a two-pronged manner. First, an original two-way blade modeling method is introduced in order to efficiently redesign any compressor blade, thus going beyond design limitations inherent to previous studies [18]. Second, this two-way blade modeling method is applied on two industrial blades: NASA rotor 37 and NASA rotor 67 (respectively a transsonic compressor blade and a fan blade) to get new insight on the relevance of the clearance consumption criterion and its applicability in the case of larger and more flexible blades such as fan blades.

The paper is organized as follows: in the second section, the redesign methodology is presented, including key quantities of interest and the blade parameterization. In the third section, the redesign of NASA rotor 37 is carried out before that of NASA rotor 67 be presented in the fourth section.

2 Redesign methodology

Figure 1 summarizes the redesign methodology proposed in this article. It can be decomposed into three steps:

modeling of the blade of interest: from a Computed Aided Design (CAD) model of the blade, called input blade, a parameter extraction procedure is used to obtain a high-fidelity parameterized model.

update of the blade: from initial blade parameters, a versatile optimization process is conducted to improve a performance criterion related to the blade's robustness to nonlinear structural interactions. At each iteration, blade parameters provided by an optimizer are used to generate a CAD model and a Finite Element (FE) mesh, and the performance criterion is computed.

dynamic analysis of optimized blade: from the optimized blade parameters, CAD model and FE mesh are generated and may be used for various dynamic analyses aiming at quantifying the actual robustness of the optimized blade to nonlinear structural interactions.

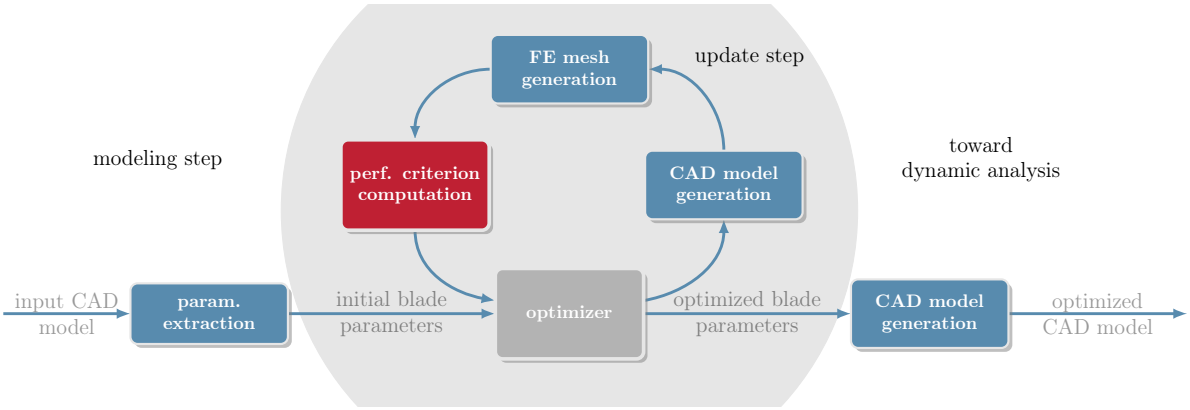

Figure 1. Description of the proposed redesign methodology.

Modeling and update steps shown in Fig. 1 are implemented in a modular automated tool using the Python 3 programming language. The open-source software package Salome 9.7[1] is used to compute CAD models and FE meshes. The open-source optimizer NOMAD v.3.9.1 [19] is chosen to manage the update step. These technological choices allow for the integration of the tool in both academical and industrial contexts.

The complete redesign process relies on a blade parameterization inspired from a previous publication [18] and presented in the first subsection. All blocks in Fig. 1 are then presented in dedicated subsections.

2.1 Blade parameterization

The blade is modeled by n_{sec} sections resulting from the intersections of the blade with conical surfaces; whenever the conicity of the surface is null, the term cylindrical section is preferred. The blade depicted in Fig. 2 with $n_{\text{sec}} = 3$ has two conical sections, at the top and hub of the blade, and one cylindrical section at midspan. The position and orientation of a section are given by stacking parameters whereas the shape of each unwrapped section, called profile, is described by profile parameters. All section parameters are listed in Table 1.

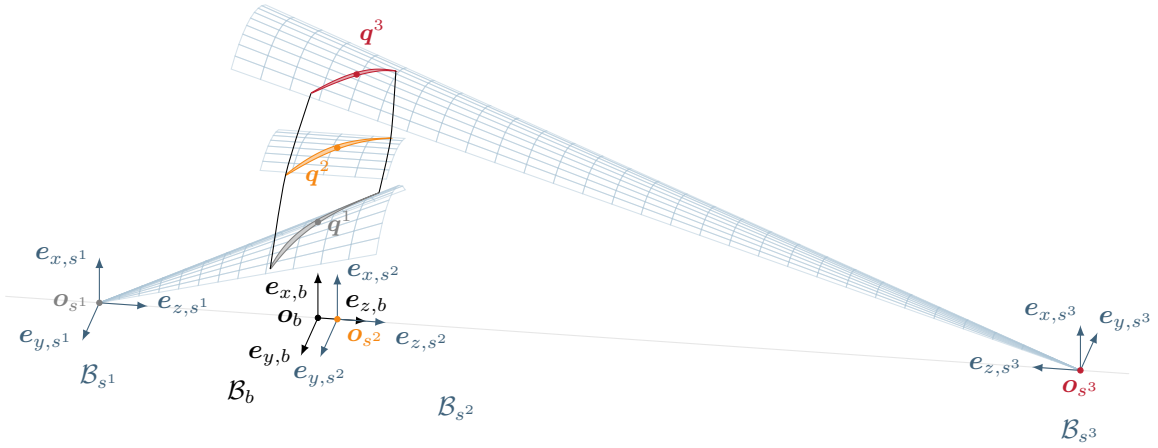

Figure 2. Blade basis $\mathcal{B}_b$, wrapped surface bases $\mathcal{B}_{s^1}, \mathcal{B}_{s^3}$ of conical sections and $\mathcal{B}_{s^2}$ of a cylindrical section.

[1] https://www.salome-platform.org/

Table 1. Section parameters.

type	name	symbol
stacking	radius	r^i
	lean angle	$\Delta\theta^i$
	sweep distance	Δz^i
	conicity	γ^i
	stagger angle	λ^i
profile	suction point abscissa	$s^i_{u,p}$
	suction point ordinate	$s^i_{v,p}$
	pressure point abscissa	$p^i_{u,p}$
	chord	c^i
	thickness	t^i
	major radius upper ellipse	$r^i_{LE^+}$
	major radius lower ellipse	$r^i_{LE^-}$
	circle radius	r^i_{TE}
	blade inlet angle	ϕ^i_{LE}
	inlet upper wedge angle	$\psi^i_{LE^+}$
	inlet lower wedge angle	$\psi^i_{LE^-}$
	blade outlet angle	ϕ^i_{TE}
	outlet upper wedge angle	$\psi^i_{TE^+}$
	outlet lower wedge angle	$\psi^i_{TE^-}$

2.1.1 Notations

Sections are numbered with index $i \in \{1, ..., n_{\text{sec}}\}$ from the hub to the top of the blade. For each section i, a reference point is denoted by $\boldsymbol{q}^i$. Different bases are required to define the section parameters. The coordinates of a point $\boldsymbol{m}$ in a three-dimensional Cartesian basis $\mathcal{B}_\bullet = (\boldsymbol{o}_\bullet, \boldsymbol{e}_{x,\bullet}, \boldsymbol{e}_{y,\bullet}, \boldsymbol{e}_{z,\bullet})$ are denoted $\boldsymbol{m}|_{R_\bullet} = (m_{x,\bullet}, m_{y,\bullet}, m_{z,\bullet})$. Its coordinates in the related cylindrical basis $\mathcal{B}'_\bullet = (\boldsymbol{o}_\bullet, \boldsymbol{e}_{r,\bullet}, \boldsymbol{e}_{\theta,\bullet}, \boldsymbol{e}_{z,\bullet})$ are denoted $\boldsymbol{m}|_{R'_\bullet} = (m_{r,\bullet}, m_{\theta,\bullet}, m_{z,\bullet})$ In a two-dimensional Cartesian basis $\mathcal{P}_\bullet = (\boldsymbol{o}_\bullet, \boldsymbol{e}_{u,\bullet}, \boldsymbol{e}_{v,\bullet})$, the coordinates are denoted $\boldsymbol{m}|_{P_\bullet} = (m_{u,\bullet}, m_{v,\bullet})$.

The blade is described in a blade basis $\mathcal{B}_b(\boldsymbol{p})$, so that an arbitrary blade point $\boldsymbol{p}$ belongs to the $(\boldsymbol{o}_b, \boldsymbol{e}_{x,b})$ axis and the flow circulates along the $(\boldsymbol{o}_b, \boldsymbol{e}_{z,b})$ axis. The basis is depicted in Fig. 2, where $\boldsymbol{p} = \boldsymbol{q}^1$. Wrapped surface bases $\mathcal{B}_{s^i}$ related to the conical surfaces $i \in \{1, ..., n_{\text{sec}}\}$ are positioned such as represented in Fig. 2 (sections 1 and 3). For cylindrical sections (section 2 in figure), $\boldsymbol{o}_{s^i}$ is located on the $(\boldsymbol{o}_b, \boldsymbol{e}_{x,b})$ axis so that a chosen blade point $\boldsymbol{k}^i$ satisfies $k^i_{x,s^i} = 0$ ($\boldsymbol{k}^2 = \boldsymbol{q}^2$ in Fig. 2). Each section i may be unwrapped in a plane described by a two-dimensional basis $\mathcal{P}_{s^i}$; the unwrapping of a conical section is illustrated in Fig. 3. Finally, all profiles are defined in a common two-dimensional profile basis $\mathcal{P}_p$ depicted in Fig. 4. Each profile is positioned such that a leading edge point $\boldsymbol{a}^i|_{\mathcal{P}_p}$ is at the origin and a trailing edge point $\boldsymbol{b}^i|_{\mathcal{P}_p}$ on the abscissa axis. The reference point $\boldsymbol{q}^i$ is defined as the barycenter of the profile in $\mathcal{P}_p$.

2.1.2 Stacking parameters

The stacking of sections in $\mathcal{B}_b$ is controlled by 5 parameters listed in Table 1 and depicted in Fig. 3. The radius r^i defines the absolute radial position of $\boldsymbol{q}^i$ whereas the lean angle $\Delta\theta^i$ and the sweep distance Δz^i control its position with respect to the hub section:

$$r^i = q^i_{r,b}, \quad \Delta\theta^i = q^i_{\theta,b} - q^1_{\theta,b}, \quad \Delta z^i = q^i_{z,b} - q^1_{z,b}. \tag{1}$$

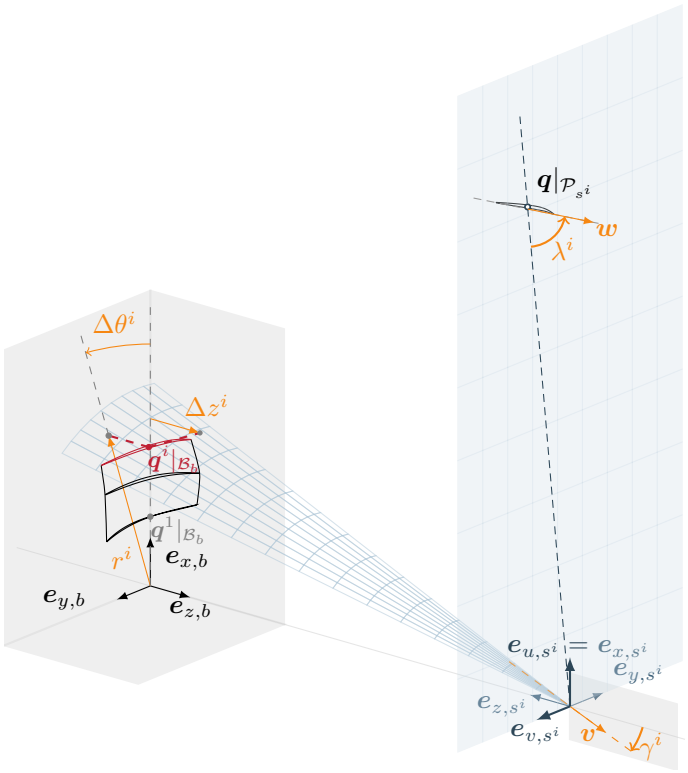

Figure 3. Representation of the stacking parameters.

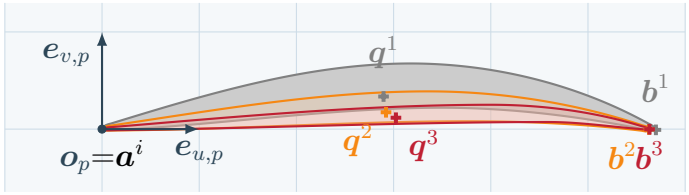

Figure 4. Profiles basis $\mathcal{P}_p$.

The conicity angle γ^i of the wrapped surface is defined by the oriented angle between the $(\boldsymbol{o}_b, \boldsymbol{e}_{z,b})$ axis and a generatrix vector $\boldsymbol{v}$ such that $v_{y,b} = 0$ and $v_{z,b} > 0$. The wrapped surface is a cylinder when $\gamma^i = 0$. Finally the stagger angle λ^i controls the orientation of the section on the wrapped surface. It is defined in the basis $\mathcal{P}_{s^i}$ from the chord vector $\boldsymbol{w}^i = \boldsymbol{b}^i|_{\mathcal{P}_{s^i}} - \boldsymbol{a}^i|_{\mathcal{P}_{s^i}}$:

$$\lambda^i = \begin{cases} \widehat{(\boldsymbol{q}^i|_{\mathcal{P}_{s^i}}, \boldsymbol{w}^i)}[\pi] & \text{for a conical section,} \\ \widehat{(\boldsymbol{e}_{u,s^i}, \boldsymbol{w}^i)} & \text{for a cylindrical section.} \end{cases} \tag{2}$$

2.1.3 Profile parameters

The profile modeling is inspired from a published parameterization [18]; seven curves are used to describe a profile in $\mathcal{P}_p$, see Fig. 5. Suction and pressure sides are modeled by two cubic splines each (①, ②, ③, ④). The leading edge is modeled by two distinct ellipsoidal arcs (⑤, ⑥) meeting at point $\boldsymbol{a}^i$, fixed at the origin, see Fig. 5b. The ratio of the ellipsis axes is fixed such as $r^i_{LE^+}/r^i_{LE^-} = 2$. The trailing edge is modeled by a unique circular arc (⑦) whose center lies on the abscissa axis, see Fig. 5c. The crossing point of the arc and the axis is denoted by the point $\boldsymbol{b}^i$. The $\mathcal{G}^1$ continuity of the profile is ensured and horizontal tangents are imposed at suction point $\boldsymbol{s}^i$ and pressure

point $\boldsymbol{p}^i$. The curves are thus parameterized by 14 profile parameters defined in $\mathcal{P}_p$ in Fig. 5 and listed in Table 1.

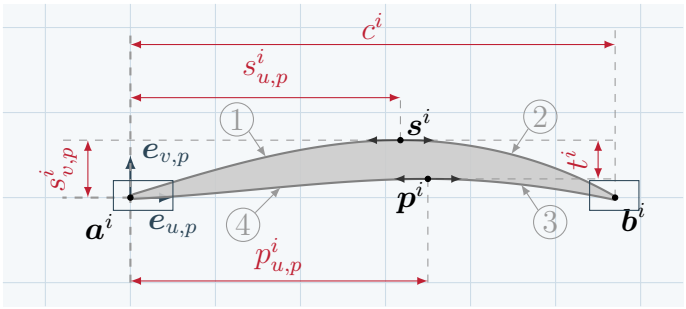

(a) blade profile

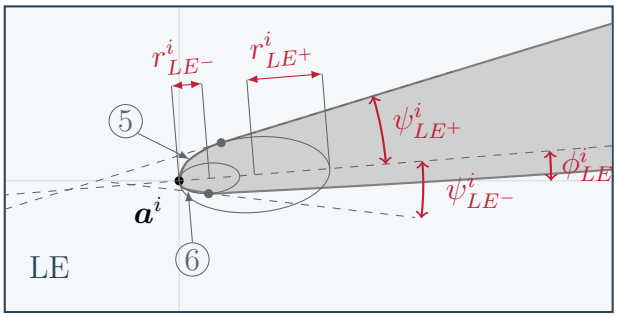

(b) zoom on the leading edge

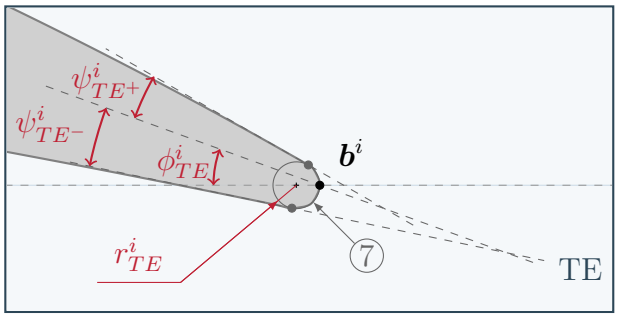

(c) zoom on the trailing edge

Figure 5. Representation of profile parameters.

2.2 Parameter extraction

The CAD model of the input blade is provided in a basis $\mathcal{B}_{CAD}$ such that the blade rotates in the forward direction around the $(\boldsymbol{o}_{CAD}, \boldsymbol{e}_{z,CAD})$ axis. The point $\boldsymbol{p}$ is chosen as the blade point with the smallest coordinate along $\boldsymbol{e}_{z,CAD}$ and used to position the blade in the blade basis $\mathcal{B}_b(\boldsymbol{p})$ depicted in Fig. 2. Sections are computed in $\mathcal{B}_b$ from the intersections of the blade with n_{sec} conical surfaces. Stacking parameters are then determined during the unwrapping of the sections, and profile parameters are finally identified by solving an optimization problem. All blade parameters are independent from the choice of point $\boldsymbol{p}$. For illustration purposes, the parameter extraction is used in the following to obtain a parameterized model of rotor 37 with $n_{\text{sec}} = 3$.

2.2.1 Intersection with conical surfaces

Each wrapped surface may be generated from the conicity parameter γ^i and the radius b^i of the surface in the plane $(\boldsymbol{o}_b, \boldsymbol{e}_{r,b}, \boldsymbol{e}_{\theta,b})$. The quantities γ^1, γ^n, b^1, b^n related to hub and top sections are computed semi-automatically: from a mesh of the blade generated automatically, several nodes on the top and hub faces are selected by the user. A linear regression is conducted on each face from the selected points to determine the required quantities. The quantities γ^i and b^i related to other sections are computed by a linear interpolation between sections 1 and n_{sec}:

$$\gamma^i = \gamma^1 + (\gamma^{n_{\text{sec}}} - \gamma^1)\frac{i-1}{n_{\text{sec}}-1} \quad \forall i \in \{1, ..., n_{\text{sec}}\}, \tag{3}$$

$$b^i = b^1 + (b^{n_{\text{sec}}} - b^1)\frac{i-1}{n_{\text{sec}}-1} \quad \forall i \in \{1, ..., n_{\text{sec}}\}. \tag{4}$$

From Eqs. (3) and (4), n_{sec} surfaces are thus generated and the intersections with the blade are computed. This results in n_{sec} point clouds finely describing the contour of each section.

2.2.2 Determination of stacking parameters

The conicity γ^i is known for all sections from Eq. (3) and the determination of $\boldsymbol{q}^i$ is required to compute the remaining stacking parameters. The point cloud of each section is projected from $\mathcal{B}_b$ to $\mathcal{P}_p$. To perform these changes of basis, the knowledge of some points and vectors in $\mathcal{B}_b$ and $\mathcal{P}_{s^i}$ are required. The determination of these quantities is not detailed for the sake of conciseness. Then, the reference point $\boldsymbol{q}^i|_{\mathcal{P}_p}$ is computed. The coordinates $\boldsymbol{q}^i|_{\mathcal{P}_{s^i}}$ are obtained to compute the stagger angle λ^i defined in Eq. (2). Finally, from the coordinates $\boldsymbol{q}^i|_{\mathcal{B}_b}$ of all sections, the parameters r^i, $\Delta\theta^i$ and Δz_i are deduced according to Eq. (1).

2.2.3 Identification of profile parameters

The point cloud of each section i in $\mathcal{P}_p$ is sampled with approximately 200 points and denoted target profile T^i. For each section, the profile parameters $\boldsymbol{x} \in \mathbb{R}^{14}$ are identified by minimizing an error function $e(\boldsymbol{x})$ between the parameterized profile defined by $\boldsymbol{x}$ and the target profile T^i. The error function, issued from a previous work [18], is defined as:

$$e(\boldsymbol{x}) = 0.9\bar{d}(\boldsymbol{x}) + 0.1|\delta p(\boldsymbol{x})|, \tag{5}$$

where $\bar{d}(\boldsymbol{x})$ is the average distance between the points of the target and parameterized profiles and $\delta p(\boldsymbol{x})$ is the relative difference in perimeters between profiles.

Because of the discretization of the profiles, the gradient of the error function is not known analytically and additional computational efforts would be required to estimate it. Consequently, the identification problem is solved with the derivative-free algorithm Mads [20] embedded in NOMAD [19]. To ensure the robustness of the parameter identification, the required bounds of the optimization problem and the vector of initial parameters $\boldsymbol{x}^0$ are computed relatively to the points of T^i. The suction point coordinates $(s^i_{u,p}, s^i_{v,p})$ and the chord c^i are directly computed from T^i and thus kept constant in the optimization process. This reduces the dimension of the identification problem to 11.

To solve the problem, 1500 evaluations of $e(\boldsymbol{x})$ are allowed and the default parameters of NOMAD are used. The parameterized profile identified for the hub section of rotor 37 is depicted in Fig. 6. The asymptotic convergence of Mads was checked for 17 profiles issued from rotor 37: 1500 evaluations–which requires about 5 min of computation time- are found sufficient to converge to low error values comparable to those observed in previous works [18].

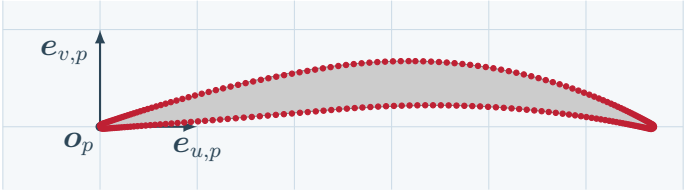

Figure 6. Target profile (●) and parameterized profile (▭) with $e(\boldsymbol{x}) \simeq 0.22$ for the hub section of rotor 37.

2.3 CAD and FE model generation

The model generation is illustrated in the following from blade parameters describing 3 sections of rotor 37. These parameters were obtained with the extraction procedure described in the previous section.

2.3.1 Generation and stacking of sections

The profile parameters are used to generate the profile of all sections $i \in \{1, ..., n_{\text{sec}}\}$ in $\mathcal{P}_p$, see Fig. 4. The profiles are finely discretized in n_{sec} point clouds from which the barycenter $\boldsymbol{q}^i|_{\mathcal{P}_p}$ of each section is computed. All point clouds are then projected from basis $\mathcal{P}_p$ to $\mathcal{B}_b$ using the stacking parameters. For the sake of conciseness, the change of basis equations are not detailed.

2.3.2 CAD model computation

Point clouds in $\mathcal{B}_b$ are imported in Salome in order to generate a CAD model. The generation methodology is inspired from a published tool [21] whose robustness has been greatly improved. Each point cloud is interpolated by two distinct cubic splines describing pressure and suction sides. To facilitate the subsequent generation of a regular mesh, each spline is split in its middle: the contour of each section is thus modeled by four splines, depicted in different gray levels in Fig. 7a. Four spline surfaces spanning the blade height are consequently generated to model the side faces ①, ②, ③, ④ of the blade, see Fig. 7b. Based on a given adaptive tolerance, coincident edges are located and sewed to generate a single side surface meeting the $\mathcal{G}^2$ regularity requirement. Finally, the hub and top blade faces are generated by hole filling and all faces are used to generate the CAD model depicted in Fig. 7c.

2.3.3 FE model computation

The side surface of the blade is meshed with quadrangle elements, defined by the discretization of each edge depicted in Fig. 7c in n_h elements. The hub and top faces are meshed with triangles. Considering the sensitivity of the nonlinear dynamic simulations conducted in the following to the submesh of the top face, the areas of the triangle are controlled to ensure the regularity of this submesh. The blade volume is thus meshed with quadratic pentahedrons, see Fig. 7d. According to a thorough convergence analysis, the value $n_\mathrm{h} = 38$ is considered acceptable for the considered nonlinear simulations.

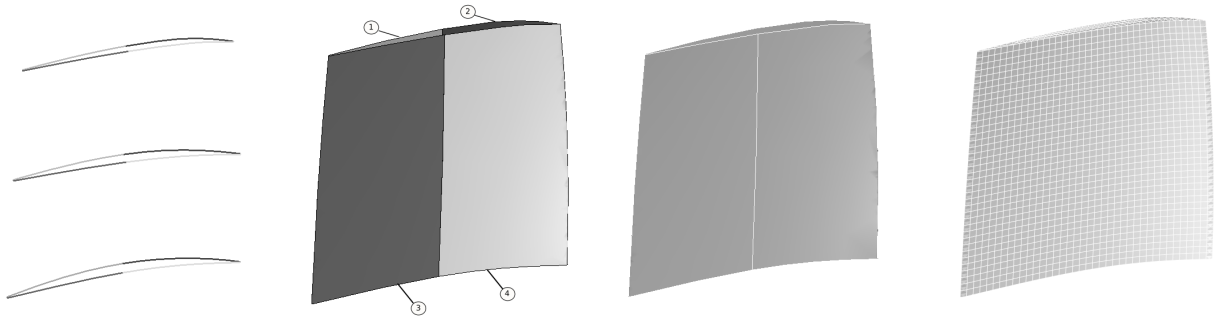

(a) section contours **(b)** side faces **(c)** CAD model **(d)** FE mesh

Figure 7. CAD model and FE mesh generation.

2.4 Performance criterion

Considering the modularity of the process depicted in Fig. 1, any performance criterion may be considered to drive the iterative update step, which is key for the versatility of the proposed methodology.

In the context of blade-tip/casing contact interactions, lower amplitudes of vibration have been predicted for blades optimized with respect to the clearance consumption [17, 18]. From this observation, clearance consumption is considered in this work as a surrogate quantity to efficiently assess the robustness of a blade to contact interactions and chosen as performance criterion.

The clearance consumption represents the variation of the blade-tip/casing clearance for a given node u when the blade vibrates along one of its free-vibration modes, indexed by p. Modal shapes of mode p are scaled in such a way that tangential displacement of the leading edge are $+\tau$ and $-\tau$. From both shapes, the minimal blade-tip/casing clearance at node u is retained and denoted $c_{u,p}$. Hence, the clearance consumption $\delta c_{u,p}$ is computed as:

$$\delta c_{u,p} = c_u - c_{u,p}, \tag{6}$$

where c_u is the blade-tip/casing clearance at node u at rest. A value $\delta c_{u,p} > 0$ indicates that the clearance is *consumed*, *i.e.* reduced, along mode p, which is assumed to be detrimental as contacts occur along the blade-tip.

2.5 Optimization

The optimization process conducted during the update step aims at minimizing a performance criterion $f(\boldsymbol{x})$ with respect to a vector of optimization variables $\boldsymbol{x}$, *i.e.* some blade parameters allowed to vary during the process. A generic formulation of the problem is given as:

$$\begin{aligned} &\min_{\boldsymbol{x}} f(m(\boldsymbol{x})) \\ &\boldsymbol{l} \leq \boldsymbol{x} \leq \boldsymbol{u}, \end{aligned} \tag{7}$$

where m is a mapping function from optimization variables $\boldsymbol{x}$ to blade parameters $\boldsymbol{y}$ and $\boldsymbol{l}$, $\boldsymbol{u} \in \mathbb{R}^4$ are bound vectors.

To limit the numerical cost of the optimization, a reduced number of parameters are chosen in this work as optimization variables. To preserve aerodynamic properties, profile parameters of the initial blade are fixed. Considering the influence of lean and sweep quantities on the blade-tip/casing interactions considered in this work [13], the vector of optimization variables is defined as $\boldsymbol{x} = \{\Delta z^3, \Delta\theta^3, \Delta z^5, \Delta\theta^5\}$, as blades are modeled with 5 sections in the following. The quantities $\Delta z^2, \Delta\theta^2, \Delta z^4, \Delta\theta^4$ are computed by a quadratic interpolation of the sweep distance and lean angle at sections 1 (null by definition), 3 and 5. All other stacking parameters are kept identical to the initial blade. A mapping function is defined according to the previous choices and the complete vector $\boldsymbol{y}$ of blade parameters may be computed as $\boldsymbol{y} = m(\boldsymbol{x})$.

In the context of this study, the update step aims at minimizing the clearance consumption: $f(\boldsymbol{y}) = \delta c_{u,p}(\boldsymbol{y})$. The gradient of the clearance consumption is not analytically known and cannot be easily estimated. Besides, for a vector of blade parameters $\boldsymbol{y}$, the computation time of the CAD model, FE model and clearance consumption is about 45 s on a standard PC. While the clearance consumption is a relatively inexpensive criterion, computation times are likely to increase with more sophisticated nonlinear contact criteria. Consequently, Problem (7) may be seen as a blackbox optimization problem. The latter is solved with the derivative-free algorithm Mads [20] based on a direct search mechanism. It is well-suited for inequality constrained blackbox optimization involving time-consuming simulations and handles situations in which the model generation returns an error or fails. The Mads implementation NOMAD v.3.9.1 is used with default parameters and the optimization is stopped after a maximum of 400 simulations of the clearance consumption.

3 Redesign of NASA rotor 37

NASA rotor 37 is a transsonic compressor blade for which a peak in vibration amplitude was numerically identified when blade-tip/casing contacts occur over an angular speed range located close to the intersection of its first bending mode and the fourth engine order [22]. As a case study for the proposed redesign methodology, it is here optimized with respect to its clearance consumption. The initial blade model is detailed in the first subsection before the blade's dynamics as it undergoes structural contacts be investigated in the second subsection. The third subsection describes the update of the blade, and the resulting optimized blades are thoroughly analyzed in the last subsection.

3.1 Modeling of the initial blade

The parameter extraction procedure described in Sect. 2.2 is applied on the input blade model NASA rotor 37. Parameterized models with $n_{\text{sec}} = \{2, 3, 5, 9\}$ are computed. The fidelity of these models with respect to the input blade is thoroughly assessed using several geometric criteria, such as volume and profile shape, and dynamic criteria, including eigenfrequencies and dynamic response to contact simulations. Based on these results—not detailed here for the sake of conciseness—the 5-section parameterized model is chosen as the stating point of the update step.

As in previous works [13, 22], the material properties of a 18Ni 200-grade maraging steel are used for all rotor 37 models: Young's modulus $E = 180$ GPa, Poisson's ratio $\nu = 0.3$, and density $\rho = 8000$ kg·m^{-3}. FE meshes of all considered blade models feature 20781 nodes and 6384 elements. The analysis of modal shapes of initial blade reveals that the first two free-vibration modes are respectively the first bending (1B) and first torsion (1T) modes. An error of 0.06% is observed on the first eigenfrequency with respect to the initial blade. A mean error of less than 2% is reached on the first ten eigenfrequencies.

3.2 Dynamic analysis of the initial blade

In order to assess the amplitudes of vibration of the blade as it undergoes blade-tip/casing contacts, time integration simulations [23] are carried out over a wide angular speed range surrounding the interaction of interest: $\omega \in [1250, 1550]$ rad·s^{-1}. For each angular speed, computations are run assuming null initial conditions and over 200 revolutions in order to reach a steady-state. For the sake of numerical efficiency, the Craig-Bampton component mode synthesis technique [24] is used to compute a reduced-order model. Eight boundary nodes evenly spaced along the blade-tip are considered along with ten modal degree of freedom. A modal structural damping is considered with a coefficient $\xi = 1 \times 10^{-3}$ on the first three modes and $\xi = 5 \times 10^{-3}$ for the other modes. Centrifugal effects are neglected.

With respect to the contact scenario, a deformed rigid casing with two privileged contact areas is considered. Parameters issued from a previous publication are used [22]; in particular, blade-tip/casing clearance at rest is 5×10^{-4} m. For the considered angular speed range, highest displacements are observed at the leading edge, thus motivating the choice of this particular location in the remainder.

3.2.1 Nonlinear Frequency Response Curve

The Nonlinear Frequency Response Curve (NFRC) depicted in Fig. 8 is computed from the infinite norm of the global displacement $\boldsymbol{d}_{LE}$ at the leading edge over the last blade revolution. In comparison to the linear resonance predicted at $\omega_{1B}/4$, contact nonlinearities induce a shift of the nonlinear resonance towards higher values—a phenomenon known as contact stiffening. Other interactions are evidenced at each bound of the considered angular speed range. While their analysis goes beyond the scope of this paper, they feature significantly lower amplitudes of vibration thus justifying *a posteriori* the emphasis on the interaction involving mode 1B and the fourth engine order.

The severity of the simulated interaction is underlined by the predicted amplitudes of vibration. While amplitudes of vibration higher than 10 mm may not be physically relevant due to the small perturbation assumption related to the use of a linear finite element model, they indicate that severe damage (including cracks) are likely to occur and motivate the proposed redesign.

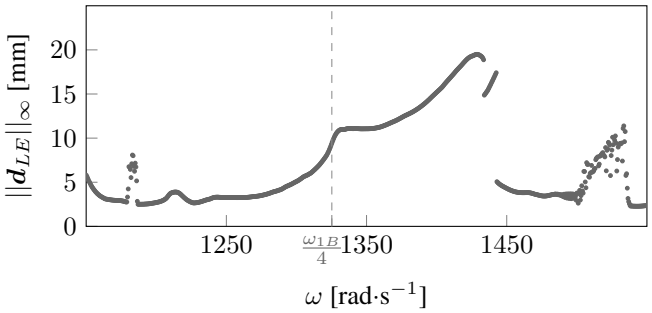

Figure 8. NFRC of initial rotor 37 blade (——).

3.2.2 Modal contributions

As a complement to the NFRC pictured in Fig. 8, modal contributions—computed over the last two periods of each time response—are depicted in Fig. 9. More specifically, this plot represents the relative contribution of each free-vibration mode of index p, looking at the infinite norm of the contribution of each mode over the last two simulated periods. A color code from white (no significant response) to black (maximal response) allows to identify the main contributors in the dynamic response of the blade throughout the considered angular speed range. Overall, there is a clear domination of the first free-vibration mode (1B) in the blade's dynamics. The only other non-negligible contribution that is computed relates to the first torsion mode (1T), over narrow angular speed ranges, such as in the vicinity of $\omega = 1325$ rad·s^{-1}.

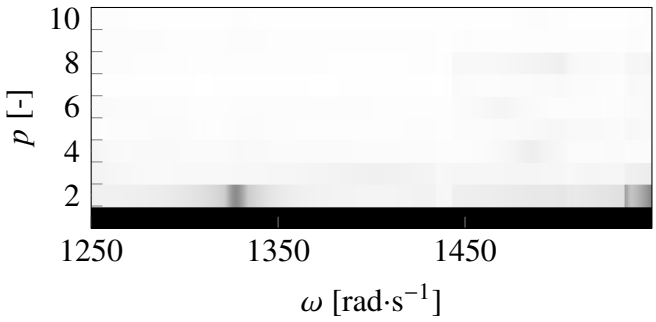

Figure 9. Normalized modal contributions of initial rotor 37 blade (from 0 (□) to 1 (■)).

3.3 Update of the blade

Two instances—A and B—of optimization problem (7) are considered and listed in Table 2. For instance A, the clearance consumption along the first bending mode is used as performance criterion, similarly to what was done in previous work [18]. For instance B however, the clearance consumption is computed relatively to the first torsion mode, which is the only other mode with a non negligible contribution of the blade's dynamics over the angular speed range of interest, see Fig. 9. For both instances, optimization bounds are small enough to ensure that the optimized blade features relatively small variations in comparison to the initial geometry. Based on this observation, it is assumed that the first and second free-vibration modes of iterated geometries always correspond respectively to the first bending and first torsion modes. Blades resulting from the two instances of the optimization problem are referred to as blade A and blade B in the remainder and depicted in Fig. 10.

Table 2. Optimization instances for rotor 37.

instance	perf. criterion	bounds	
		Δz^3, Δz^5	$\Delta\theta^3$, $\Delta\theta^5$
A	$c_{LE,1B}$	$[-2\text{mm}, 2\text{mm}]$	$[-1.5°, 1.5°]$
B	$c_{LE,1T}$	$[-2\text{mm}, 2\text{mm}]$	$[-1.5°, 1.5°]$

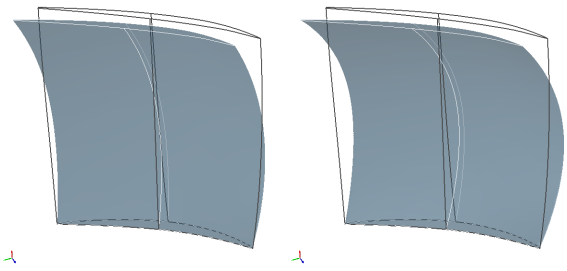

(a) blade A **(b)** blade B

Figure 10. CAD models of optimized blades (■) with respect to initial rotor 37 blade(□).

3.3.1 Clearance consumption variations

Clearance consumptions of initial and optimized blades are computed for a tangential displacement of the leading edge computed from $\tau = 2$ mm. The relative variation of clearance consumption $\Delta(\delta c_{u,p})$ of an optimized blade

Table 3. Clearance consumption variations with respect to rotor 37.

blade	node u	$\Delta(\delta c_{u,1B})$ [%]	$\Delta(\delta c_{u,1T})$ [%]
A	1	-98	-55
	2	-84	-45
	3	-85	-17
	4	-78	2203
	5	-66	-79
	6	-74	-77
	7	-61	-59
	8	-68	-66
B	1	-48	-91
	2	-66	-75
	3	-72	-43
	4	-86	2850
	5	-95	-81
	6	-94	-87
	7	-86	-85
	8	-96	-92

with respect to the initial blade is defined by:

$$\Delta(\delta c_{u,p}) = \frac{\delta c'_{u,p} - \delta c_{u,p}}{\delta c_{u,p}} \times 100 \quad [\%], \tag{8}$$

where the clearance consumptions $\delta c'_{u,p}$ and $\delta c_{u,p}$ are respectively related to the optimized blade and initial blade. For instances A and B, significant improvements of the performance criterion are achieved for the optimized blades within the allowed simulation budget: for blade A, $\Delta(\delta c_{LE,1B}) = -98\%$ and for blade B $\Delta(\delta c_{LE,1T}) = -91\%$.

Table 3 depicts the relative variation of clearance consumptions of all boundary nodes u for the two first modes. Values from -100% to 100% are colored from blue to red and values above 100% are colored in red. Blue cells highlight strong improvements in terms of clearance consumption. Targeted optimized values are circled in white. It has been checked that very large positive results stem from near zero values of the initial blade clearance consumption and are thus not relevant; the corresponding cells are drawn in white. Despite the fact that the optimized quantities $c_{LE,1B}$ or $c_{LE,1T}$ are very localized—as they relate to the leading edge only and to the first bending or torsion modes—, it is found that clearance consumptions are significantly improved all along the blade-tip. As an example, for blade A, optimizing $c_{LE,1B}$ yields strong improvements in $c_{u,1B}$ for all boundary nodes u as well as in $c_{u,1T}$ for most boundary nodes. Similarly, for blade B, optimizing $c_{LE,1T}$ leads to significant improvements at all boundary nodes along both modes.

3.3.2 Partial conclusion

Modal contributions and the NFRC obtained for the considered contact configuration underline that the dynamic response of the initial blade is dominated by its first bending mode throughout the angular speed range of interest. In addition, the optimization of the clearance consumption on the leading edge leads to a global improvement of the clearance consumptions of the first two modes for all boundary nodes. In this context, the use of a performance criterion limited to $c_{LE,1B}$ or $c_{LE,1T}$, despite of its lack of versatility, seems well-suited to the redesign of the NASA rotor 37 blade, which is in good agreement with previous observations [17].

3.4 Dynamic analysis of the optimized blade

Contact simulations are carried out for optimized blades A and B with the numerical strategy used in Sect. 3.2. The NFRC related to the global displacement of the leading edge are depicted in Fig. 11 for both the optimized and the initial blades. Other than the blade models themselves, all simulation parameters are identical. The unavoidable modification of the blades' eigenfrequencies due to the update of their geometries yields a shift in terms of nonlinear resonance. For instance, the nonlinear resonance predicted for $\omega \simeq 1440$ rad·s^{-1} with the initial blade is shifted to $\omega \simeq 1280$ rad·s^{-1} for blade A, respectively $\omega \simeq 1260$ rad·s^{-1} for blade B. Interestingly, corresponding amplitudes of vibration are cut from about 20 mm on the initial blade to about 5 mm on blade A. Overall, it is evidenced that there is a very significant reduction of the amplitudes of vibration throughout the considered angular speed range. While an in-depth analysis may be required to fully understand these phenomena, it seems that other interactions predicted for the initial blade—see, for instance, the increased amplitudes for $\omega \geq 1500$ rad·s^{-1}—vanish with both optimized blades.

The redesign methodology presented in the previous sections allows for the first time to redesign existing compressor blades and it is numerically evidenced that, in the case of NASA rotor 37, very significant gains can be made. Also, results presented in this section are in line with previous publications [17] and confirm that the clearance consumption may be a very relevant quantity to optimize when designing compressor blades robust to contact interactions.

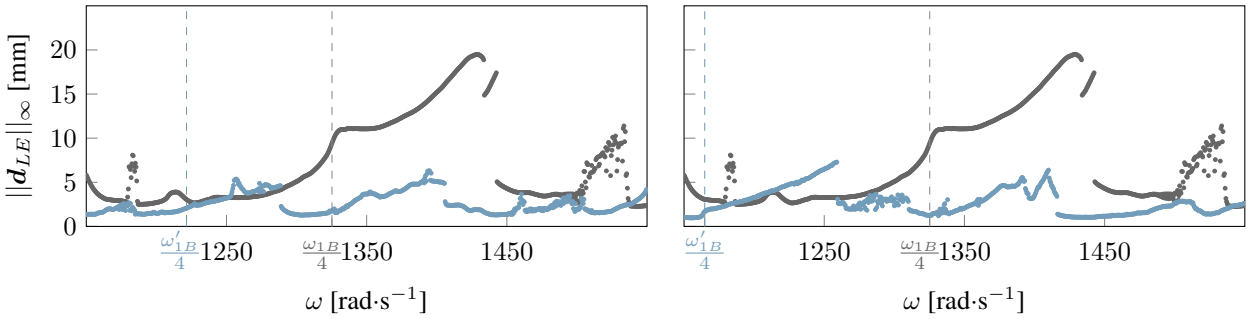

(a) blade A **(b)** blade B

Figure 11. NFRC of optimized blades (——) and initial rotor 37 blade (——).

4 Redesign of NASA rotor 67

Taking advantage of the proposed redesign methodology, it is proposed to assess the relevance of the clearance consumption performance criterion to other types of blades, such as fan blades. As a matter of fact, contrary to what may be observed for small high-pressure compressor blades [16] and transsonic compressor blades such as NASA rotor 37, fan blades are significantly more flexible, featuring lower eigenfrequencies, which imply that their dynamic response to nonlinear structural interactions may be particularly complex.

The blade of interest in this section is a fan blade of NASA rotor 67, the 22 blades first-stage rotor of a two-stage fan [25]. This rotor has served as a standard validation case for three-dimensional viscous flow prediction methods, it was also recently studied in the context of blade-tip/casing contact interactions [26]. The input CAD models of both rotor 67 and rotor 37 used in this work are freely available online[2].

The nominal speed of NASA rotor 67 is $\omega = 1680$ rad·s^{-1}. Among the speeds of interest below this angular speed, the crossing between the first bending mode and the second engine order, reached for $\omega = \omega_{1B}/2$, was recently identified as a critical speed in the context of blade-tip/casing interactions [26]. Accordingly, in the following, a wide angular speed range including both the critical speed $\omega_{1B}/2$ and the nominal speed is considered: $\omega \in [900,\ 1700]$ rad·s^{-1}.

[2] https://lava-wiki.meca.polymtl.ca/public/modeles/accueil

4.1 Modeling of the initial blade

A parameterized model of the initial blade is computed with the parameter extraction procedure described in Sect. 2.2. Five sections are found sufficient to obtain a high fidelity parameterized blade. A generic titanium (Ti-6V-4Al) is used with the following material properties: Young's modulus $E = 108$ GPa, Poisson's ratio $\nu = 0.34$, and density $\rho = 4400$ kg·m^{-3}. FE meshes computed for the initial and optimized blades feature 20393 nodes and 6232 elements. According to the analysis of modal shapes of the initial blade, the first three free-vibration modes are the first bending (1B), the second bending (2B) and first torsion (1T) modes.

4.2 Dynamic analysis of the initial blade

Blade-tip/casing contact simulations are carried out with the same numerical strategy as used for rotor 37 in Sect. 3.2. For the sake of numerical efficiency, a reduced-order model featuring a 8-node contact interface and $\eta = 10$ constraint modes is computed. Blade-tip/casing clearances at rest are set to 4×10^{-4} m according to NASA report [25] and other parameters of the contact scenario are unchanged with respect to those of the previous simulations with rotor 37. Because the highest displacements are observed at the leading edge all over the considered angular speed range, most of the presented results refer to this node in the following.

4.2.1 Nonlinear Frequency Response Curve

The NFRC of the initial blade is depicted in Fig. 12. Contrary to the results obtained with rotor 37, see Fig. 8, the NFRC of rotor 67 exhibits very sophisticated vibration patterns. In particular, areas where clouds of points are drawn—such as for $\omega \in [1400,\ 1500]$ rad·s^{-1}—may indicate that computed solutions are not periodic or feature a period that does not correspond to one blade revolution. In addition, there is no clear sign of a nonlinear resonance specifically related to the first bending mode.

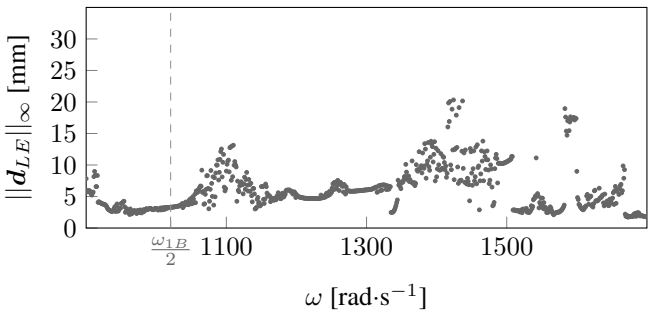

Figure 12. NFRC of initial rotor 67 blade (——).

4.2.2 Modal contributions

Same as for rotor 37, relative modal contributions are computed over the last two blade rotations and normalized as explained in Sect. 3.2. The resulting map drawn in Fig. 13 underlines the intricacy of the blade's dynamic response: several free-vibration modes, as high as the seventh mode, have significant contributions.

While the first bending mode is overall dominant, there are some angular speed ranges over which its contribution vanishes and where other modes drive the blade's response. This is observed for both the second bending mode ($\omega \simeq 1580$ rad·s^{-1}) and the first torsion mode ($\omega \simeq 900$ rad·s^{-1} and $\omega \simeq 1350$ rad·s^{-1}). Overall, the first three free-vibration modes (1B, 2B and 1T) drive the blade's response.

Put together, the NFRC and the map of modal contributions underline the significant challenge that constitutes the redesign of a blade such as rotor 67 in order to enhance its robustness to blade-tip/casing contact interactions. Indeed, it exhibits an intricate dynamics that involves a large number of free-vibration modes.

4.3 Update of the blade

Three instances—C, D and E—of optimization problem (7) are considered and presented in Table 4. For each instance, the clearance consumption at the blade's leading edge is optimized with respect to a different free-vibration

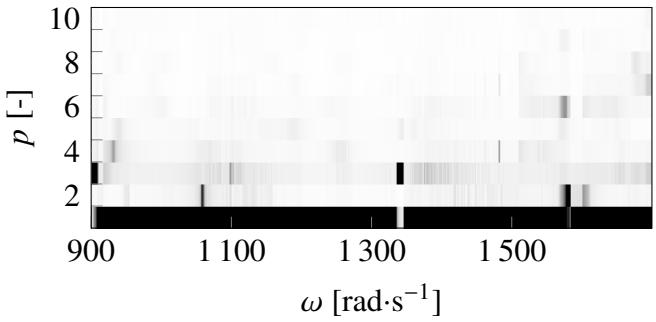

Figure 13. Normalized modal contributions of initial blade rotor 67 (from 0 (□) to 1 (■)).

mode: 1B, 2B and 1T, in agreement with the fact that those three modes are dominant in the blade's response throughout the considered angular speed range, see Fig. 13. Optimized blades are respectively denoted as blades C, D and E and depicted in Fig. 14. Because the blade height is about twice rotor 37's height, bounds of the optimization variables related to sweep distance are increased.

Table 4. Optimization instances for rotor 67.

instance	perf. criterion	bounds	
		Δz^3, Δz^5	$\Delta\theta^3$, $\Delta\theta^5$
C	$c_{LE,1B}$	$[-3\text{mm}, 3\text{mm}]$	$[-1.5°, 1.5°]$
D	$c_{LE,2B}$	$[-3\text{mm}, 3\text{mm}]$	$[-1.5°, 1.5°]$
E	$c_{LE,1T}$	$[-3\text{mm}, 3\text{mm}]$	$[-1.5°, 1.5°]$

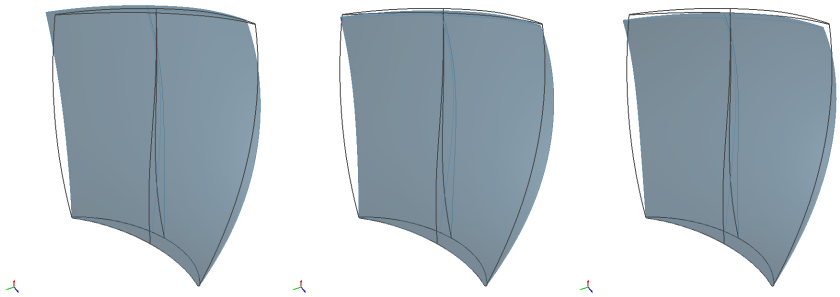

(a) blade C **(b)** blade D **(c)** blade E

Figure 14. CAD models of optimized blades (■) with respect to initial rotor 67 blade (□).

4.3.1 Clearance consumption variations

Clearance consumptions at each contact node along the first three free-vibration modes are computed for a tangential displacement of the leading edge given by the value $\tau = 4$ mm. Variations of clearance consumptions between optimized and initial blades are given in Tab. 5. For each instance, the optimized quantity is significantly improved: $\Delta(\delta c_{LE,1B}) = -73\%$ for blade C, $\Delta(\delta c_{LE,2B}) = -98\%$ for blade D and $\Delta(\delta c_{LE,1T}) = -58\%$ for blade E. However, it is patent that the optimization of the clearance consumption at the leading edge along a single mode leads to mixed results overall. At best, see blade D, the clearance consumption is significantly improved at all nodes of the blade-tip but only for the free-vibration mode to which relates the performance criterion: mode 2B. For blade

C however, the optimization of the clearance consumption at the leading edge along mode 1B only yields minor improvements at the trailing edge (−19 %). Even worse, for blade E, the optimization of the clearance consumption at the leading edge for mode 1T leads to an increase of the clearance consumption at the mid-chord. Overall, in the case of rotor 67, it is found that improving the clearance consumption along a single free-vibration mode implies a deterioration of this same quantity on other free-vibration modes.

Table 5. Clearance consumption variations with respect to rotor 67.

blade	node u	$\Delta(\delta c_{u,1B})$ [%]	$\Delta(\delta c_{u,2B})$ [%]	$\Delta(\delta c_{u,1T})$ [%]
C	1	-73	-52	3
	2	-36	-45	10
	3	-40	-55	70
	4	-26	-46	-15
	5	-26	-53	-11
	6	-21	-49	-10
	7	-18	-47	-10
	8	-19	-58	-10
D	1	45	-98	-20
	2	-87	-77	-12
	3	-84	-94	49
	4	-57	-76	-68
	5	-55	-87	-60
	6	-40	-77	-48
	7	-33	-73	-45
	8	-34	-91	-53
E	1	291	60	-58
	2	21	-14	-19
	3	26	21	163
	4	-63	-32	5
	5	-73	-9	-35
	6	-82	-38	-84
	7	-66	-52	-90
	8	-66	-11	-84

4.3.2 Partial conclusion

Contrary to rotor 37, the optimization of the clearance consumption at the leading edge for the first bending mode does not lead to a global improvement of clearance consumptions on other modes and boundary nodes. This may be explained by blade geometry and the high number of free-vibration modes contributing to the blades' dynamics on the considered angular speed range. In this context, the redesign of rotor 67 with respect to contact interaction based on a localized clearance consumption criterion appears more challenging.

4.4 Dynamic analysis of optimized blades

Contact simulations are conducted on optimized blades with simulation parameters used for the analysis of the initial blade in Sect. 4.2. The resulting NFRC computed from the global displacement of the leading edge are depicted in Fig. 15.

For all optimized blades, the variation on the first eigenfrequency is small with respect to the initial blade, hence the linear resonances predicted at $\frac{\omega'_{1B}}{2}$ are close to the one of the initial blade at $\frac{\omega_{1B}}{2}$. For blade C and D, an increase in the amplitudes of vibration is observed for nearly all angular speeds with respect to the initial blade. This may be explained by the deterioration of clearance consumption on modes 1T and 1B which are likely to contribute to the blade's dynamic. For blade E, an increase in vibration amplitudes is observed for the angular speeds following the interaction, up to 1200 rad·s^{-1}. For higher angular speeds, the amplitudes are comparable to those of the initial blade. An in-depth analysis would though be required to conclude on other possible interactions. Overall, for all

optimized blades, the maximum magnitudes reached over the considered angular speed range are higher than those of the initial blade.

Contrary to instances A and B on rotor 37, for instances C, D and E, the minimization of the clearance consumption at one node along the first bending mode does not reduce the magnitude of the resonance peak related to the interaction of interest. Opposite trends in this matter observed on rotor 37 and rotor 67 may be explained by fundamentally different blades dynamic on the considered angular speed ranges. Furthermore, optimizations on rotor 67 lead to very localized improvements of clearance consumption with respect to mode and boundary node, whereas global improvements are observed for rotor 37. Besides, the severity of clearance consumption of initial blades, estimated by normalizing clearance consumption by the prescribed tangential displacement τ, is significantly higher for rotor 37 than for rotor 67. In this context, it is coherent that diminution of any clearance consumption for rotor 37 induces an improvement on the blade robustness. Thus, presented results indicate that the relevance of a local clearance consumption as performance criterion is highly dependent on the dynamics of the initial blade.

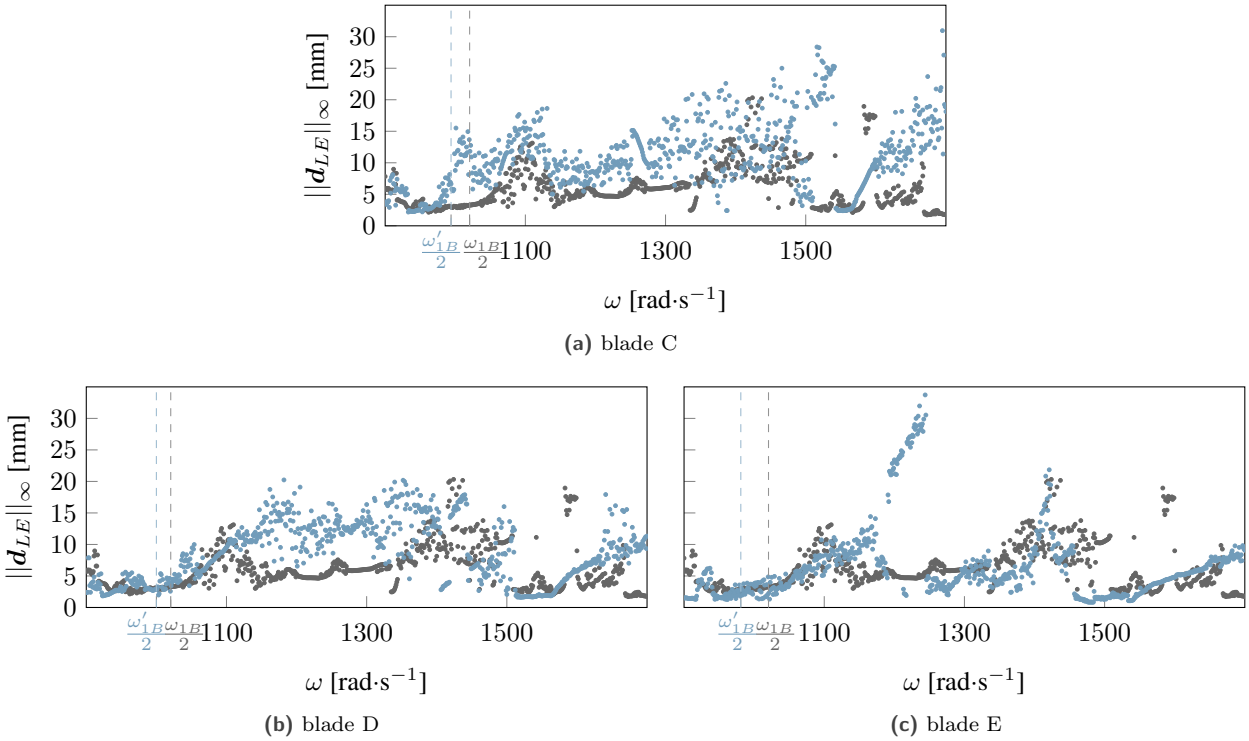

(a) blade C

(b) blade D

(c) blade E

Figure 15. NFRC of optimized blades (——) and initial rotor 67 blade (——).

5 Conclusion

This article presents a redesign methodology dedicated to compressor blades with the intent of providing designers with new tools to enhance blades' robustness to nonlinear structural interactions. A versatile parameter extraction procedure is proposed to obtain high-fidelity parameterized models of existing blades. As a proof-of-concept, redesign is conducted to mitigate blade-tip/casing contact interactions on two distinct blade models: NASA rotor 37 and rotor 67.

Thanks to this methodology, the relevance of a performance criterion based on clearance consumption is carefully assessed for these different types of blades. Indeed, this work brings new insights on the relevance of the clearance consumption as a surrogate quantity to assess blade-tip/casing contacts robustness when considering a single node and a single free-vibration mode. Presented results suggest that when the dynamics of the blade is mainly driven by one free-vibration mode, for certain types of blades, such as rotor 37, a minimization of the performance

criterion may lead to a global improvement on all nodes and contributing modes. However, when the initial blade exhibits an intricate dynamics involving significant contributions of several free-vibration modes, such as rotor 67, optimized blades are likely to feature other types of interactions that, in the end, will yield significant—potentially larger—amplitudes of vibration. As a first step toward a more versatile surrogate quantity, one could consider extending the computation of clearance consumption to several nodes along the blade-tip for the first two or three free-vibration modes. The computation may also be extended by accounting for centrifugal effects.

More generally, the demonstration that the proposed redesign methodology is applicable in the context of blade-tip/casing contacts opens avenues to its application to other types of nonlinear structural interactions. Its structural dynamics oriented focus, and the fact that it could easily be extended to a full sector of a bladed disk, could also make it suitable for identifying blade shapes best-suited for intentional mistuning patterns for instance.

Acknowledgments

This research was supported by the Canada Research Chairs Program (Funder ID: 10.13039/ 501100001804), the Natural Sciences and Engineering Research Council of Canada (discovery grant RGPIN-2020-04448) and the FRQNT (PBEEE scholarship).

References

[1] J. Noël and G. Kerschen. Nonlinear system identification in structural dynamics: 10 more years of progress. Mechanical Systems and Signal Processing Vol. 83 (2017), 2–35. DOI: 10.1016/j.ymssp.2016.07.020.

[2] L. Pacyna, A. Bertret, A. Derclaye, L. Papeleux, and J.-P. Ponthot. Implementation of a Rig Test for Rotor/Stator Interaction of Low-Pressure Compressor Blades and Comparison of Experimental Results With Numerical Model. *Proceedings of the ASME Turbo Expo 2020: Turbomachinery Technical Conference and Exposition.* Vol. 11: Structures and Dynamics: Structural Mechanics, Vibration, and Damping; Supercritical CO2. Virtual, Online., 2020. DOI: 10.1115/GT2020-14266.

[3] M. Krack, L. Salles, and F. Thouverez. Vibration Prediction of Bladed Disks Coupled by Friction Joints. Archives of Computational Methods in Engineering Vol. 24, No. 3 (2017), 589–636. DOI: 10.1007/s11831-016-9183-2. OAI: hal.archives-ouvertes.fr/hal-01825517.

[4] E. P. Petrov. Multiharmonic Analysis of Nonlinear Whole Engine Dynamics With Bladed Disc-Casing Rubbing Contacts. *Proceedings of the ASME Turbo Expo 2012: Turbine Technical Conference and Exposition.* Vol. 7: Structures and Dynamics, Parts A and B. Copenhagen, Denmark, 2012, pp. 1181–1191. DOI: 10.1115/GT2012-68474.

[5] C. M. Firrone, S. Zucca, and M. M. Gola. The effect of underplatform dampers on the forced response of bladed disks by a coupled static/dynamic harmonic balance method. International Journal of Non-Linear Mechanics Vol. 46, No. 2 (2011), 363–375. DOI: 10.1016/j.ijnonlinmec.2010.10.001.

[6] K. Prabith and I. R. P. Krishna. The numerical modeling of rotor–stator rubbing in rotating machinery: a comprehensive review. Nonlinear Dynamics Vol. 101, No. 2 (2020), 1317–1363. DOI: 10.1007/s11071-020-05832-y.

[7] H. Ma, F. Yin, Y. Guo, X. Tai, and B. Wen. A review on dynamic characteristics of blade–casing rubbing. Nonlinear Dynamics Vol. 84, No. 2 (2016), 437–472. DOI: 10.1007/s11071-015-2535-x.

[8] S. M. Pourkiaee and S. Zucca. A Reduced Order Model for Nonlinear Dynamics of Mistuned Bladed Disks With Shroud Friction Contacts. Journal of Engineering for Gas Turbines and Power Vol. 141, No. 1 (2018). DOI: 10.1115/1.4041653.

[9] A. Millecamps, J.-F. Brunel, P. Dufrenoy, F. Garcin, and M. Nucci. Influence of Thermal Effects During Blade-Casing Contact Experiments. *Proceedings of the ASME 2009 International Design Engineering Technical Conferences and Computers and Information in Engineering Conference.* Vol. 1: 22nd Biennial Conference on Mechanical Vibration and Noise, Parts A and B. San Diego, United States, 2009, pp. 855–862. DOI: 10.1115/DETC2009-86842. OAI: hal.archives-ouvertes.fr/hal-01223060.

[10] C. Padova, J. Barton, M. Dunn, and S. Manwaring. Experimental Results From Controlled Blade Tip-Shroud Rubs at Engine Speed. Journal of Turbomachinery Vol. 129, No. 4 (2007), 713–723. DOI: 10.1115/1.2720869.

[11] R. Agromayor, N. Anand, J.-D. Müller, M. Pini, and L. O. Nord. A Unified Geometry Parametrization Method for Turbomachinery Blades. Computer-Aided Design Vol. 133 (2021), 102987. DOI: 10.1016/j.cad.2020.102987. OAI: resolver.tudelft.nl/uuid:5a9751f2-1c4c-4a2d-8ad8-9799bf3164d8.

[12] Y. Zhou, Y. Song, T. Xing, Y. Wang, Q. Zhang, L. Shao, F. Du, and S. Ding. Parametric modeling method for integrated design and manufacturing of radial compressor impeller. International Journal of Advanced Manufacturing Technology Vol. 112, No. 3-4 (2021), 1007–1021. DOI: 10.1007/s00170-020-06331-5.

[13] E. Piollet, F. Nyssen, and A. Batailly. Blade/casing rubbing interactions in aircraft engines: numerical benchmark and design guidelines based on nasa rotor 37. Journal of Sound and Vibtaion Vol. 460 (2019), 114878. DOI: 10.1016/j.jsv.2019.114878. OAI: hal.archives-ouvertes.fr/hal-02281666.

[14] C. J. Hulme, S. W. Fiebiger, and J. Szwedowicz. Axial Compressor Blade Failure, Design Modification, and its Validation. *Proceedings of the ASME Turbo Expo 2015: Turbine Technical Conference and Exposition*. Turbo Expo: Power for Land, Sea, and Air. Montreal, Canada, 2015. DOI: 10.1115/GT2015-43312.

[15] S. Nitschke, T. Wollmann, C. Ebert, T. Behnisch, A. Langkamp, T. Lang, E. Johann, and M. Gude. An advanced experimental method and test rig concept for investigating the dynamic blade-tip/casing interactions under engine-like mechanical conditions. Wear Vol. 422-423 (2019), 161–166. DOI: https://doi.org/10.1016/j.wear.2018.12.072.

[16] A. Batailly, M. Legrand, A. Millecamps, S. Cochon, and F. Garcin. Redesign of a high-pressure compressor blade accounting for nonlinear structural interactions. Journal of Engineering for Gas Turbines and Power Vol. 137, No. 2 (2015), 022502. DOI: 10.1115/1.4028263. OAI: hal.archives-ouvertes.fr/hal-01120158.

[17] A. Batailly and A. Millecamps. Minimising clearance consumption: a key factor for the design of blades robust to rotor/stator interactions? *ASME Turbo Expo*. Séoul, South Korea, 2016. DOI: 10.1115/GT2016-56721. OAI: hal.archives-ouvertes.fr/hal-01618315.

[18] J. Lainé, E. Piollet, F. Nyssen, and A. Batailly. Blackbox optimization for aircraft engine bladed components featuring contact interfaces. Journal of Engineering for Gas Turbines and Power (2019). DOI: doi:10.1115/1.4042808. OAI: hal.inria.fr/hal-02059582v1.

[19] S. Le Digabel. Algorithm 909: NOMAD: Nonlinear Optimization with the MADS algorithm. ACM Transactions on Mathematical Software Vol. 37, No. 4 (2011), 44:1–44:15. DOI: 10.1145/1916461.1916468.

[20] C. Audet and J. Dennis Jr. Mesh Adaptive Direct Search Algorithms for Constrained Optimization. SIAM Journal on Optimization Vol. 17, No. 1 (2006), 188–217. DOI: 10.1137/040603371.

[21] E. Piollet and A. Batailly. *A program to compute compressor blade geometries from multiple-circular-arc parameters with sweep and lean (v1.0)[source code]*. 2019. URL: https://hal.archives-ouvertes.fr/hal-02127993.

[22] Y. Colaïtis and A. Batailly. Development of a harmonic balance method-based numerical strategy for blade-tip/casing interactions: application to NASA rotor 37. Journal of Engineering for Gas Turbines and Power (2021). DOI: 10.1115/1.4051967. OAI: hal.archives-ouvertes.fr/hal-03286205.

[23] A. Batailly, M. Legrand, A. Millecamps, and F. Garcin. Numerical-experimental comparison in the simulation of rotor/stator interaction through blade-tip/abradable coating contact. Journal of Engineering for Gas Turbines and Power Vol. 134, No. 8 (2012), 082504. DOI: doi:10.1115/1.4006446. OAI: hal.archives-ouvertes.fr/hal-00746632.

[24] R. R. Craig and M. C. C. Bampton. Coupling of Substructures for Dynamic Analyses. AIAA Journal Vol. 6, No. 7 (1968), 1313–1319. DOI: 10.2514/3.4741. OAI: hal.archives-ouvertes.fr/hal-01537654.

[25] D. C. Urasek, W. S. Cunnan, and W. Stevans. *Performance of two-stage fan with larger dampers on first-stage rotor*. Tech. rep. NASA-TP-1399. NASA Lewis Research Center, Cleveland, OH: NASA, 1979. URL: https://ntrs.nasa.gov/citations/19790015796.

[26] Y. Colaïtis. Stratégie numérique pour l'analyse qualitative des interactions aube/carter. PhD thesis. École Polytechnique de Montréal, 2021. OAI: tel.archives-ouvertes.fr/tel-03318777. URL: https://tel.archives-ouvertes.fr/tel-03318777.